coatings

MDPI

Article

# Morphology-Dependent Near-Infrared Electrochromic Properties of Tungsten Oxide

**Qingyi Huang [1,*], Yi Liang [2], Sheng Cao [2,*] and Zaishang Yang [1,*]**

[1] School of Basic Medical Science, You Jiang Medical University for Nationalities, Baise 533000, China
[2] School of Physical Science and Technology, Guangxi University, Nanning 530004, China
* Correspondence: jiayouyaggg@163.com (Q.H.); caosheng@gxu.edu.cn (S.C.); yangzaishangcc@gmail.com (Z.Y.)

**Abstract:** Vertically aligned $WO_3$ nano-architectures on the transparent conducting substrate are produced via a hydrothermal method. The results revealed that different $WO_3$ nano-architectures, including "nanoblocks", "nanosheet" and "nanobelt" structures, can be obtained by adjusting the composition of the precursor solution, that shows that solvent composition plays an important role in the adjustment of the prepared material morphology. The nanostructured array films with thicknesses of about 600 nm show remarkable enhancement of the electrochromic properties in the infrared region. The obtained $WO_3$ films have good electrochromic properties in the near-infrared range. In particular, significant optical modulation of the $WO_3$ nanosheets (72% at 1200 nm), fast switching speed (6.5 s for colored and 8.7 s for bleached), and excellent cycling stability (maintained 90.2% of the initial optical modulation after 1000 cycles). The improved electrochromic performance is mainly due to the vertically arranged structure, which makes it easier for ions to diffuse in the nanoarray, and also provides a larger surface area for charge transfer reaction. The research results provide a certain reference value for the research of electrochromic near-infrared performance.

**Keywords:** near-infrared; tungsten trioxide; morphology; electrochromism

check for updates

**Citation:** Huang, Q.; Liang, Y.; Cao, S.; Yang, Z. Morphology-Dependent Near-Infrared Electrochromic Properties of Tungsten Oxide. *Coatings* **2023**, *13*, 344. https://doi.org/10.3390/coatings13020344

Academic Editor: Flavio Deflorian

Received: 23 December 2022
Revised: 31 January 2023
Accepted: 1 February 2023
Published: 2 February 2023



## 1. Introduction

The primary energy used for buildings in the world is up to 30%–40%, which is mainly used for heating, cooling, lighting, ventilation, and household appliances [1,2]. A large part of this energy consumption is related to our inability to control the entry and exit of solar infrared light through windows. With the development of society and economy, dynamic regulation of solar light and heat flow can significantly reduce the energy consumption of buildings, and then reduce the characteristics of energy consumption, causing a global boom [3]. Electrochromic devices have attracted the attention of researchers because they can dynamically change indoor light and temperature, thereby effectively controlling solar thermal gain [4]. Electrochromism (EC) refers to the phenomenon that a material dynamically changes its optical properties (reflectivity, transmissivity, absorptivity) under applied voltage [5]. So far, the research on electrochromic properties not only focuses on the visible light, but also includes near-infrared that can change the indoor temperature. With the increasing demand for tunable near-infrared light (800–2000 nm) in solar thermal regulation, optical communication, aerospace, and military camouflage technologies, further research on infrared optical modulation is required [6,7]. In recent years, the Milliron group has studied various metal oxide nanomaterials, including doped semiconductor nanocrystals, non-stoichiometric oxides ($WO_{3-x}$), etc., as electrochromic materials for near-infrared light [8]. All the aforementioned are based on the dynamically adjusted carrier concentration in nanocrystals and capacitive adsorption of local surface plasmon resonance (LSPR) through capacitive charge injection to achieve near-infrared selective light modulation [9,10]. For doped semiconductor nanocrystals, there are inevitable inherent defects. First of all, the LSPR peak of doped metal oxides (indium tin oxide and aluminum doped

zinc oxide) is located in the near middle infrared region (1400 nm), and the wavelength below 1400 nm cannot be adjusted, while the near-infrared spectral range within 780–1400 nm accounts for more than 75% of the solar radiation, which makes the doped nanocrystals unable to modulate most of the short wave near-infrared radiation [11–13]. Secondly, the limitation of indium resources and the increase in material consumption make it more and more expensive.

Unlike doped metal nanocrystals, the LSPR absorption band of tungsten oxide nanocrystals (NCs) is distributed in the range of 780~1500 nm shortwave spectrum, which is consistent with the solar thermal energy distribution of sunlight, and is suitable for dynamic sunlight control [14]. The free carrier concentration of tungsten oxide nanocrystals is relatively low. Generally, the LSPR absorption can be improved by increasing the carrier concentration. Previous studies on $WO_3$ local surface plasmon resonance have mostly focused on non-stoichiometric tungsten oxide ($WO_{3-x}$), the tungsten oxide is unstable and requires controlled heat treatment in a weakly reducing environment, and will slowly oxidize when exposed to air at room temperature [15,16].

Inorganic electrochromic materials such as tungsten oxide have the characteristics of high colored efficiency, large light modulation range, good electrochemical reversibility, and good chemical stability [17,18]. The [$WO_6$] octahedral variable connection of tungsten oxide can generate crystalline tungsten oxide (c-$WO_3$) and amorphous tungsten oxide (a-$WO_3$) with different transport channel types [19]. c-$WO_3$ thin film has good stability because of its compact and orderly crystal structure, which has a high tolerance to volume changes caused by repeated ion insertion and removal, but the relatively long response time is not conducive to ion diffusion [20]. To overcome these shortcomings, a variety of methods have been studied, such as material compounding [21], constructing core-shell structures [22], doping ions [23], and adjusting crystallinity [24]. However, nanoarray structure is the most common effective way to improve near-infrared electrochromic performance [25,26]. Nanostructured films are known to provide more active reaction regions and increase the specific surface area, thus reducing the characteristic diffusion length of intercalated ions, and increasing the number of accessible intercalated sites [27]. Wang et al [28] synthesized hexagonal $WO_3$ (h-$WO_3$) nanorod cluster films, which achieved high electrochromic properties in the near-infrared range. Yang et al [29] prepared ordered macroporous $WO_3$ films, which improved infrared optical modulation and accelerated response time. Therefore, the design of thin films with unique nanostructures and surface morphologies is very important for rapid insertion kinetics and enhanced durability [30]. To our knowledge, there are few reports on the effect of morphological changes on the electrochromic NIR properties. In this present work, we attempted to use urea as the structure-directing agent and varied the water: ethylene glycol ratio in the solvent in order to adjust the obtained $WO_3$ layer structure and study the effect of these factors upon the near-infrared properties of the prepared $WO_3$ thin films. The results show that the electrochromic property of the $WO_3$ nanosheets is superior to the $WO_3$ nanoblocks and nanoribbons, including faster kinetics ($\tau_c$ = 6.5 s, $\tau_b$ = 8.7 s), high coloration efficiency (70 $cm^2$ $C^{-1}$) and good cycling stability (90.2% capacity retention after 1000 electrochemical reactions). This study provides a new way to study the near-infrared electrochromism of inorganic materials with different morphologies.

## 2. Experimental Section

### *2.1. Materials*

Hydrochloric acid (HCl, 36%) was purchased from Chengdu Kelong Reagent Co., Ltd., (Chengdu, China). Zinc perchlorate was from Shanghai Bohr Chemical Reagent Co., Ltd., (Shanghai, China). Tungstic acid ($H_2WO_4$) was purchased from Shanghai Macklin Biochemical technology Co., Ltd., (Shanghai, China). Sodium tungstate ($Na_2WO_4 \cdot 2H_2O$), hydrogen peroxide ($H_2O_2$, 30%), ethylene glycol, and urea were all procured from Guangdong Guanghua technology Co. Ltd., (Guangdong, China). All reagents and chemicals above were used as received without further purification. The substrate for the elec-

trodes is commercial FTO-glass supplied by Foshan Jingjiexin with a sheet resistance of 10 Ω square$^{-1}$.

### 2.2. Preparation of $WO_3$ Seed Layer

A total of 1 g of $Na_2WO_4 \cdot 2H_2O$ is dissolved in 25 mL of deionized water. After $Na_2WO_4 \cdot 2H_2O$ is completely dissolved in water, HCl (3 mol/L) is added dropwise. At this time, $Na_2WO_4 \cdot 2H_2O$ is converted into $H_2WO_4$ precipitation until no precipitation is generated in the solution, and HCl addition is stopped. Rinse the sediment with deionized water several times in the ice bath. Finally, 2 mL of 30% $H_2O_2$ is dropped into the precipitate to form a transparent sol, which is spun onto the FTO glass.

### 2.3. Preparation of the $WO_3$ Films

Tungstic acid is dissolved in 30% hydrogen peroxide, stirred and heated to 95 °C; after the solution becomes transparent, dilute with deionized water to a precursor solution with a concentration of 0.05 M. A total of 3.75 mL of precursor solution, 1.25 mL of hydrochloric acid (3 mol/L) and 1.2 mmol of urea are measured and added to the mixed solvent (15 mL) of ethylene glycol and deionized water with different volume ratios (1:1, 2:1, 3:1). The FTO conductive glass coated with the seed layer is placed into the precursor solution of ethylene glycol and deionized water with the volume ratio of 1:1, 2:1 and 3:1, respectively, for hydrothermal growth, and the reaction is maintained at 120 °C for 3 h. After the reaction is complete, let the temperature cool down to the same temperature as room temperature. Then take out the glass, wash it with water and ethanol one by one, and then put it into an oven for drying. Before further characterization, all the synthesized films were annealed in a box furnace at 400 °C for 30 min to enhance the adhesion of the films. The three samples recorded in this experiment are EG-1, EG-2 and EG-3, which correspond to the tungsten oxide films synthesized in the mixed solvent of ethylene glycol and deionized water at the volume ratio of 1:1, 2:1 and 3:1, respectively.

### 2.4. Characterization

The crystal structure of tungsten oxide is analyzed by X-ray diffraction (XRD, Nishiku Corporation, Tokyo, Japan). All electrochromic characterizations are performed using an AUTOLAB PGSTAT204 electrochemical workstation (Switzerland Vantone LTD., Switzerland). The electrochromic of the electrode is measured in 1 M $Zn(ClO_4)_2$/PC electrolyte (Shanghai Bohr Chemical Reagent Co., Ltd. Shanghai, China). The three-electrode system consisted of the $WO_3$ film synthesized with EG-1, EG-2 and EG-3 as working electrode (Jingjie Xin Glass Co., Ltd., Guangzhou, China), and Zn sheet (Weng Hou Metal Material Firm, Shushan District, Hefei City, China) as reference electrode and the counter electrode. The study of electrochromic properties of the $WO_3$ films includes in situ transmission spectroscopy, chronometry, and cyclic voltammetry, which are carried out at AVANTES spectrometer (AvaSpec-ULS2048CL-EVO, Beijing Avantis Technology Co., Ltd., Beijing, China) and AU-TOLAB PGSTAT204 electrochemical workstation, with a wavelength range of 380 nm to 2500 nm. During the electrochemical reaction process, the voltage applied to the electrochromic films is controlled by the connected AUTOLAB PGSTAT204 electrochemical workstation.

## 3. Results and Analysis

### 3.1. Morphology and Structure of the $WO_3$ Films

To determine the crystal structure and possible phase transitions under different hydrothermal conditions, XRD diffraction analysis was carried out. Figure 1 shows the XRD patterns of different $WO_3$ nanostructures prepared by the hydrothermal method. It can be seen from the Figure that the main crystal planes of the $WO_3$ films are (100), (002), (110), (200), and (202). With the addition of ethylene glycol (the total volume of water and ethylene glycol was 15 mL), the $WO_3$ nanostructure did not change. The diffraction peaks of the $WO_3$ films on the FTO conductive glass substrate correspond to the standard card

JCPDS Card no. 70-4176. After removing the characteristic peaks of the FTO conductive glass substrate, all the characteristic peaks of the prepared $WO_3$ films are consistent with the hexagonal phase h-$WO_3$ (hexagonal, JCPDS No. 85-2460). Under hydrothermal conditions, urea is absorbed on the surface parallel to the c-axis, thus forming a strong energy barrier, and the control crystal grows mainly along the (100) and (200) planes. Therefore, the (100) and (200) peaks of the $WO_3$ films are significantly enhanced, indicating that the $WO_3$ films are highly oriented to the substrate surface. As the intercalation host of $H^+$, $Li^+$, $Na^+$, $K^+$, and other univalent ions, h-$WO_3$ has been widely studied for preparing hexagonal tungsten bronze $M_xWO_3$ that modulates near-infrared light [31].

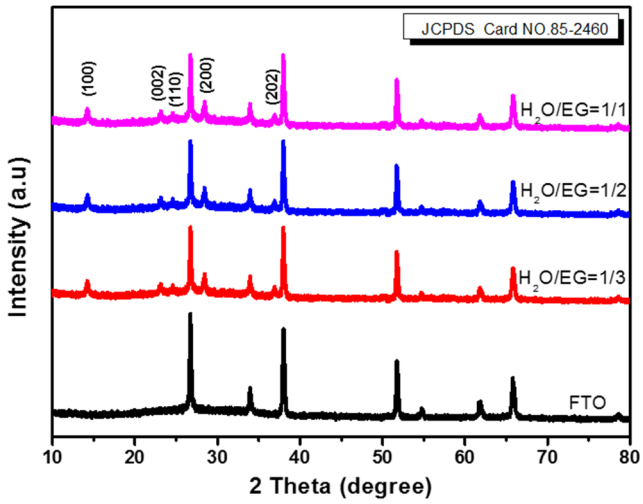


**Figure 1.** XRD pattern of h-$WO_3$ thin films prepared by hydrothermal method.

The surface microstructure of the electrode material was studied by field emission scanning electron microscopic studies. Figure 2 shows the surface morphology and cross-sectional thickness of the $WO_3$ films on FTO; the surface morphology of $WO_3$ can be changed by solvent ratio. It appears that when the solvent ratio of $H_2O$/EG is 1/1, vertically homogeneous nanoblocks were grown, and the thickness of the nanoblocks was about 20 nm (Figure 2a,b). As the solvent ratio of $H_2O$/EG becomes 1/2, as is shown in Figure 2c,d, the $WO_3$ films transform from nanoblocks to nanosheets. This is because the larger $WO_3$ nanoblocks are easy to grow, while the smaller $WO_3$ nanoblocks are more likely to dissolve and disappear due to their higher specific surface energy. This led to a large decrease in the density of the $WO_3$ nanoblocks, which results in the evolution of the nanoblocks into nanosheets, and the thickness of the nanosheets is around 16 nm. When the solvent ratio of $H_2O$/EG is 1/3 (Figure 2e,f), due to the high surface energy of the nanosheets and the consequent instability, the curling process occurs and leads to the bending of the nanosheets, and the vertically arrayed nanosheets become curved nanoribbon arrays. The average diameter of the nanoribbons is reduced to about 14 nm, but the nanoribbons are easy to peel off. As can be seen from the above results, with the increase of ethylene glycol, the morphology evolution of the films follows the process of "nanoblocks-nanosheets- nanoribbons". In addition, the cross-sectional view shows that the thickness of all $WO_3$ films is about 600 nm (Figure 2b,d,f). Scheme 1 is the formation process of "nanoblocks-nanosheet-nanobelts" by changing the ratio of water to ethylene glycol in solvent under hydrothermal conditions.

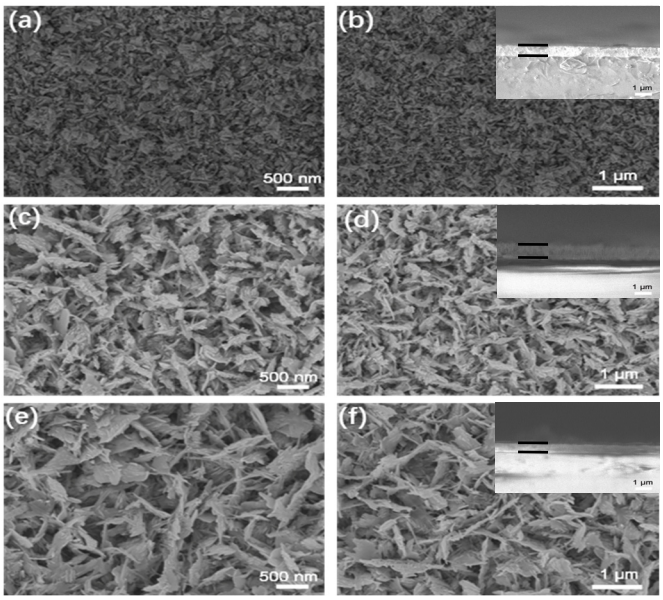


**Figure 2.** SEM images of the $WO_3$ films prepared with different solvent ratios. (**a**,**b**) $H_2O/EG = 1/1$, (**c**,**d**) $H_2O/EG = 1/2$, (**e**,**f**) $H_2O/EG = 1/3$. Insets in b, d, and f are cross-sectional view SEM images of the corresponding samples.

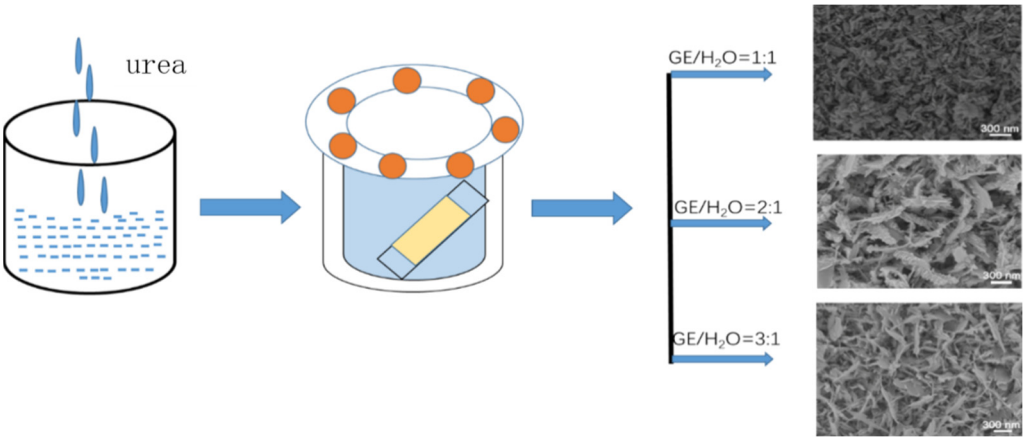


**Scheme 1.** Schematic diagram of the formation process of the $WO_3$ nanoblock, nanosheet, and nanobelt by changing the ratio of water to ethylene glycol in the solvent under hydrothermal conditions.

### *3.2. Electrochemical and Electrochromic Properties*

In order to study the electrochemical properties of the film, the voltammogram (CV) was measured at a scanning rate of 20 mV $s^{-1}$ in the voltage range of 0.2–1.2 V (vs. Zn). The zinc sheet is connected to the counter electrode and reference electrode of the electrochemical workstation, and 1 M Zn $(ClO_4)_2$/PC is used as the electrolyte. Figure 3a depicts the cyclic voltammograms (CVs) of $WO_3$ films. It is observed that the $WO_3$ nanoblocks and nanosheets exhibit larger voltametric areas than those for the $WO_3$ nanoribbons, indicating that the $WO_3$ nanoblocks and nanosheets have more active sites that can effectively participate in redox reactions and more ions are stored in the active species during the EC process [26]. Furthermore, compared with the $WO_3$ nanoribbons, the $WO_3$ nanoblocks and nanosheets have faster electrochemical kinetics and electron transport during electrochemical reactions, indicating faster ion diffusion in these films. To study the relationship between different morphology of the $WO_3$ films and response speed. The chronoampere response curves of the $WO_3$ films were tested at 1.2 V and 0.2 V potentials (Figure 3b). In the electrochromic process, the peak current generated is due to the double injection/extraction

of electrons and ions. After this process is complete, the current slowly decreases and finally remains stable. It is worth mentioning that, compared with the $WO_3$ nanoblocks and nanoribbons, the $WO_3$ nanosheet shows a faster current density change rate, indicating that the entire electrochemical reaction in the $WO_3$ nanosheet is faster, which is of great significance for improving the speed of electrochromic response. To further analyze the electrochemical kinetics of $WO_3$ films, electrochemical impedance spectroscopy (EIS) measurements were performed in the bleached state. EIS was measured at an open circuit potential of 5 mV and frequencies from 1 Hz to 100 kHz (Figure 3c). High frequency semicircles and low frequency lines comprise all EIS spectrum regions. The high frequency semicircle is the charge transfer resistance at the electrode/electrolyte interface, and the low frequency area tilting straight line represents the ion diffusion process in the electrode. Generally, the larger the high frequency semicircle, the larger the charge transfer resistance; the lower the slope of the low frequency line, the lower the ion diffusion rate [32,33]. Apparently, the $WO_3$ nanosheets and nanoribbons arrays exhibit smaller semicircles than the $WO_3$ nanoblocks, and the linear slope of the $WO_3$ nanosheet corresponding to the low frequency region is the steepest. The results show that $WO_3$ nanoparticles have higher reactivity and kinetics due to lower charge transfer resistance and ion diffusion resistance.

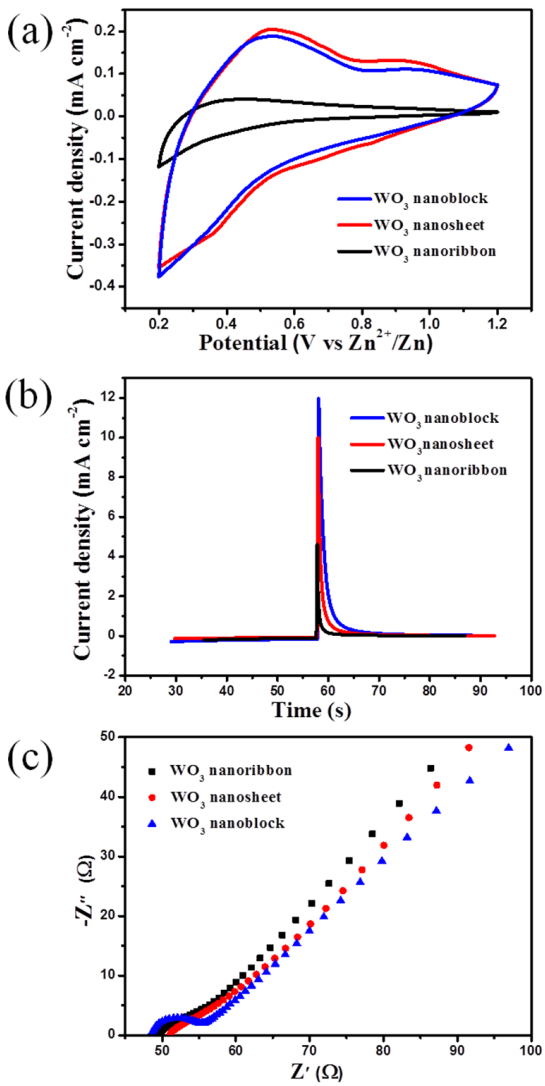


**Figure 3.** (**a**) CV curves, (**b**) Chronoamperometric curves, and (**c**) Nyquist plots of the $WO_3$ nanoblock, $WO_3$ nanosheet, and $WO_3$ nanoribbon array films.

The EC behaviors of the $WO_3$ films were investigated by constant voltage (1.2 V–0.2 V) in situ transmission tests. As shown in Figure 4a, the $WO_3$ nanosheets in the NIR region (at $\lambda$ = 1200 nm) shows a relatively high bleached transmittance ($T_b$) of 84%. When the voltage is 0.2 V, the nanosheet $WO_3$ films turn into a colored state with a transmittance of 12%. The transmittance modulation range $\Delta T$ ($\Delta T = T_b - T_c$) of the $WO_3$ nanosheets at 1200 nm was calculated to be 72%. Compared with the $WO_3$ nanosheets, the $\Delta T$ of the $WO_3$ nanoblock at the same wavelength is also 72% (Figure 4c), while that of the $WO_3$ nanoribbons is only 58.9% (Figure 4e). In the near-infrared wavelength range, the $WO_3$ nanosheets have a lower bleached state; this is because Mie scattering occurs when the wavelength of the incident light is similar to the diameter of the nanosheets [25]. Therefore, the initial transmittance of the $WO_3$ nanosheets is low. Besides transmittance modulation, response time is another important parameter for evaluating electrochromic behavior. It is defined as the time required to reach 90% of the maximum transmittance change of a particular material at a particular wavelength. In this work, the colored/bleached conversion performance was evaluated by monitoring the in situ transmittance modulation at 1200 nm under a constant voltage of 1.2 V–0.2 V. The transmittance–time response curves of the $WO_3$ films are shown in Figure 4b,d,f. For the $WO_3$ nanosheets, the colored and bleached time at 1200 nm is 6.5 s and 8.7 s, respectively, which is significantly better than that of the $WO_3$ nanoblocks (8.3 s/26.6 s) and nanoribbons (13 s/19.7 s), indicating that the $WO_3$ nanosheets have faster reaction kinetics (Table 1). The switching speed of the $WO_3$ films depends on crystal structure and microstructure. Combined with the results of chronoamperometry and in situ transmittance vs. time, it can be concluded that the $WO_3$ nanosheet arrays completed the main optical modulation in a short time after voltage switching. The fast response time of the nanosheet $WO_3$ is due to the nanosheet array structure, large active surface area, and low charge and mass transfer resistance, which is conducive to the electrolyte better entering the $WO_3$ host, shortening the diffusion distance of zinc ions in the film, and improving the electrochromic performance. The $WO_3$ nanoblock and nanobelt array require longer switching time because the active surface area is not fully used for the nanoblock structure due to the close stacking of radial nanoblocks, resulting in slow switching speed.

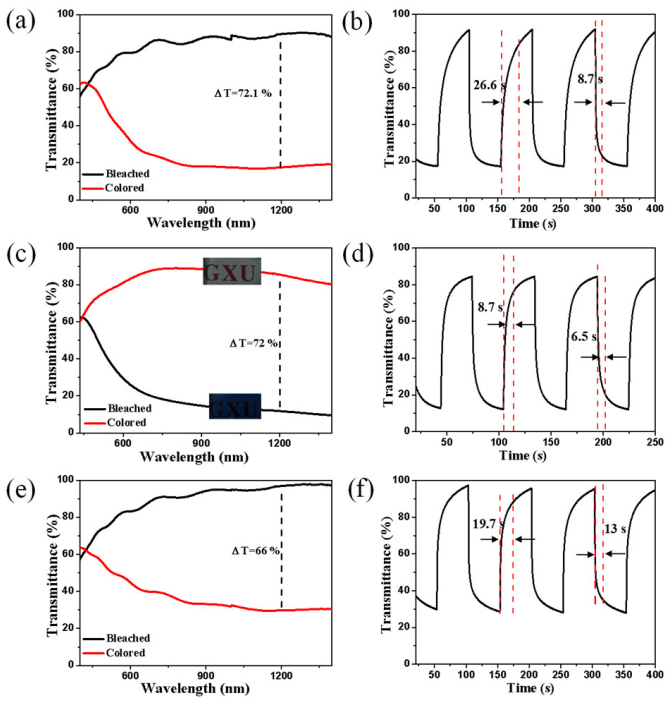


**Figure 4.** (**a**,**c**,**e**) Optical transmittance spectra, (**b**,**d**,**f**) switched response curves of the $WO_3$ nanoblocks, nanosheets, and nanoribbons array films.

**Table 1.** Near-infrared electrochromic properties of the $WO_3$ films with different morphologies.

| $WO_3$ Films | Response Time (s) | Optical Modulation (%) | Coloration Efficiency ($cm^2 \cdot C^{-1}$) |
|---|---|---|---|
| nanoblock | $\tau_c/\tau_b$: 8.7/26.6 | 72.1% | 52.8 |
| nanosheet | $\tau_c/\tau_b$: 6.5/8.7 | 72% | 70 |
| nanoribbons | $\tau_c/\tau_b$: 13/19.7 | 66% | 33.5 |

Except for the response time, the coloration efficiency (CE) is one of the inherent parameters that evaluate the performance of EC materials. CE refers to the change of optical density caused by the charge embedded in the electrochromic material per unit area in the bleached state. This can be calculated based on the following formula:

$$\Delta OD = \log(T_b/T_c) = \eta Q/A \quad (1)$$

where $\eta$ is the coloration efficiency, and A is the active area of electrochromic material. $T_b$ and $T_c$ denote transmittance in bleached and colored states, respectively. A high value of CE indicates that the electrochromic materials exhibit a large optical modulation with a small intercalation charge density [27]. Figure 5 shows the plots of OD at a wavelength of 1200 nm vs. the inserted charge density. From the slope of these curves, the CE can be calculated. The CE is found to be 52.8, 70, and 33.5 $cm^2$ $C^{-1}$ at 1200 nm for the $WO_3$ nanoblocks, nanosheets, and nanoribbons, respectively. The $WO_3$ nanosheet can maintain moderate CE. This means that a large transmittance modulation can be achieved with a small amount of charge. This is mainly due to the different modulation of the spectrum at different wavelengths. The above results are consistent with the electrochemical properties. According to the above analysis, the $WO_3$ nanosheets have greater transmittance modulation, shorter response time, and excellent CE.

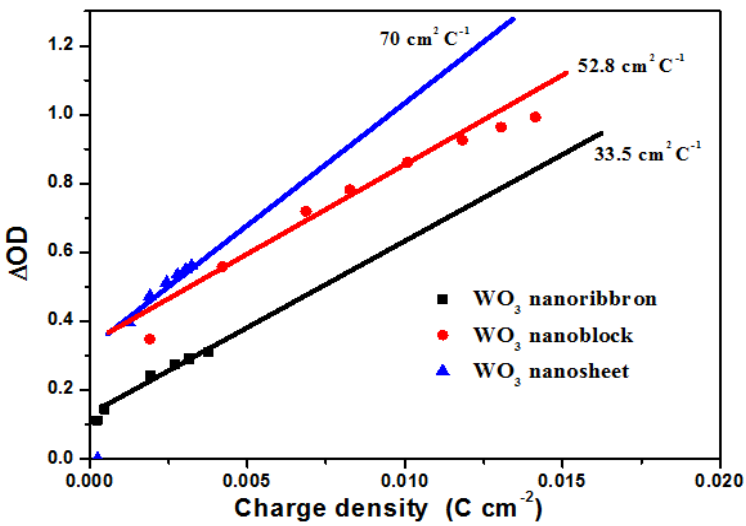


**Figure 5.** Coloration efficiency curves of the $WO_3$ nanoblock, nanosheet, and nanoribbon array films.

Cycling stability is an important parameter for practical electrochromic applications. To sum up, the $WO_3$ nanosheets have better performance; to study the cyclic stability, the cyclic voltammetry was scanned at a rate of 20 mV/s. Figure 6 records the cyclic voltammetry curves after the second cycle, 500 cycles, and 1000 cycles. After 500 and 1000 electrochemical cycles, neither the shape of the cyclic voltammetry curves nor the corresponding peak currents were significantly different, 93.3% of the initial capacity is still retained after 500 cycles, and after 1000 cycles it still retained 90.2% of its initial capacity. It is worth noting that the peak anode current slightly shifts to the anode potential with the increase in the number of cycles. Upon a continuous number of cycles, the amount

of zinc located in the reversible trap site increases and the role of the reversible trap site in the zinc insertion into the $WO_3$ film is more significant, as a result, the anodic current peak slightly shifts in the anodic direction [34,35]. It shows that the $WO_3$ nanosheets have high stability and durability under $Zn^{2+}$ intercalation/extraction. This apparent stability may be due to the adsorption of EG on the h-$WO_3$ films via hydrogen bonding or physical adsorption to make it more stable [36]. In summary, the characteristics of the $WO_3$ films NIR electrochromism, including stability and optical modulation range, are shown in Table 2. The results show that the electrochemical stability of the $WO_3$ nanosheets is better than that reported in the current study.

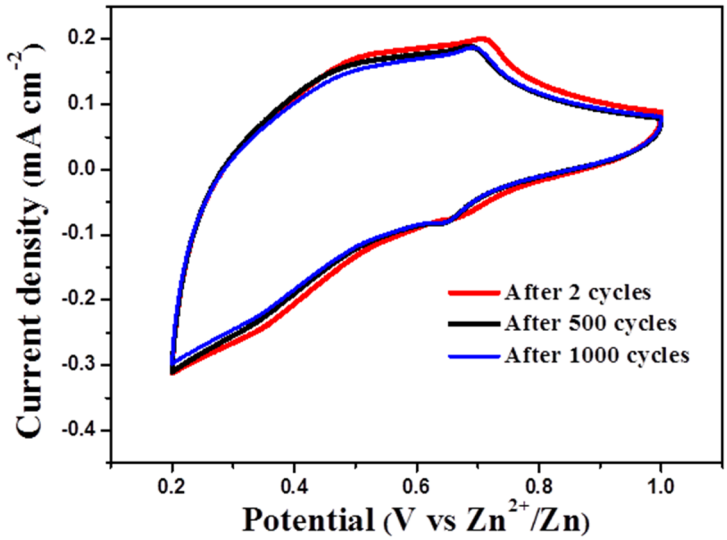


**Figure 6.** The durability test of the $WO_3$ nanosheets for 1000 cycles in the potential range from 0.2 to 1.0 V.

**Table 2.** Properties comparison of $WO_3$ thin films based on near-infrared electrochromism.

| Material | Electrolyte | Response Time (s) | Optical Modulation (%) | Stability (Cycles) | Coloration Efficiency ($cm^2$ $C^{-1}$) | Ref. |
|---|---|---|---|---|---|---|
| Hollow spherical $WO_3$ films | 0.5 M $H_2SO_4$ | $\tau_c/\tau_b$: 2.41/1.28 | 78.8% (1000 nm) | 87% (after 300 cycles) | 102.9 | [37] |
| h-$WO_3$ | 1.0 M $LiClO_4$—PC | $\tau_c/\tau_b$: 2.4/3.6 | 46% (1600 nm) | 96% (after 1000cycles) | 106.1 | [28] |
| $WO_3$ films | 1.0 M $LiClO_4$—PC | $\tau_c/\tau_b$: 5.3/3.0 | 72.5% (1000 nm) | 60% (after 1000 cycles) | 80.5 | [38] |
| c-$WO_3$@ a-$WO_3$ | 0.5 M $H_2SO_4$ | $\tau_c/\tau_b$: 3.5/4.8 | 70.3% (750 nm) | 68.5 (after 3000 cycles) | 43.2 | [20] |
| $WO_3 \cdot 2H_2O$ | 1.0 M $LiClO_4$—PC | N/A | 90% (1600 nm) | 93.7% (after 500 cycles) | 322.6 | [39] |
| $WO_3$/Ag NW films | 1.0 M $LiClO_4$—PC | N/A | 68.3% (1100 nm) | N/A | 86.9 | [40] |
| h-$WO_3$ | 1.0 M $Zn(ClO_4)_2$ | $\tau_c/\tau_b$: 6.5/8.7 | 72% (1200 nm) | 90% (after 1000 cycles) | 70 | This work |

## 4. Conclusions

In summary, $WO_3$ films with controllable morphology were prepared via a simple hydrothermal method. The results show that compared with the $WO_3$ nanoblock and nanoribbon, the $WO_3$ nanosheet has excellent electrochromic properties, including high optical modulation (72% at $\lambda$ = 1200 nm), fast response time (6.5 and 8.7 s), excellent cycle stability. In conclusion, this study demonstrates that the preparation process is simple, and the structure design is reasonable, which is a promising strategy for the preparation of high-performance $WO_3$ electrochromic materials. It is expected to be applied in the fields of smart windows, spacecraft thermal control, and infrared camouflage.

**Author Contributions:** Methodology, Y.L.; formal analysis, Q.H. and Y.L.; data curation, S.C. and Z.Y.; writing—original draft preparation, Q.H., S.C., Z.Y. and Y.L.; writing—review and editing, Q.H. and S.C. All authors have read and agreed to the published version of the manuscript.

**Funding:** Topic comes from the basic scientific research ability improvement project of young and middle-aged teachers in universities in Guangxi "Research on correlation of tungsten-based nanomaterials for photothermal treatment of tumor" project.

**Institutional Review Board Statement:** Not applicable.

**Informed Consent Statement:** Not applicable.

**Data Availability Statement:** Not applicable.

**Conflicts of Interest:** The authors declare no conflict of interest.

## References

1. Jelle, B.P. Solar radiation glazing factors for window panes, glass structures and electrochromic windows in buildings—Measurement and calculation. *Sol. Energy Mater. Sol. Cells* **2013**, *116*, 291–323. [CrossRef]
2. Wang, K.; Meng, Q.; Wang, Q.; Zhang, W.; Guo, J.; Cao, S.; Elezzabi, A.Y.; Yu, W.W.; Liu, L.; Li, H. Advances in energy-efficient plasmonic electrochromic smart windows based on metal oxide nanocrystals. *Adv. Energy Sustain. Res.* **2021**, *2*, 2100117. [CrossRef]
3. Roy, S.; Chakraborty, C. Transmissive to blackish-green NIR electrochromism in a Co(ii)-based interfacial co-ordination thin film. *Chem. Commun.* **2021**, *57*, 7565–7568. [CrossRef] [PubMed]
4. Mondal, S.; Chandra Santra, D.; Ninomiya, Y.; Yoshida, T.; Higuchi, M. Dual-redox system of metallo-supramolecular polymers for visible-to-near-IR modulable electrochromism and durable device fabrication. *ACS Appl. Mater. Interfaces* **2020**, *12*, 58277–58286. [CrossRef] [PubMed]
5. Wu, N.; Ma, L.; Zhao, S.; Xiao, D. Novel triazine-centered viologen analogues for dual-band electrochromic devices. *Sol. Energy Mater. Sol. Cells* **2019**, *195*, 114–121. [CrossRef]
6. Yang, X.; Cong, S.; Li, J.; Chen, J.; Jin, F.; Zhao, Z. An aramid nanofibers-based gel polymer electrolyte with high mechanical and heat endurance for all-solid-state NIR electrochromic devices. *Sol. Energy Mater. Sol. Cells* **2019**, *200*, 109952. [CrossRef]
7. Schott, M.; Niklaus, L.; Clade, J.; Posset, U. Electrochromic metallo-supramolecular polymers showing visible and near-infrared light transmittance modulation. *Sol. Energy Mater. Sol. Cells* **2019**, *200*, 110001. [CrossRef]
8. Kim, J.; Ong, G.K.; Wang, Y.; LeBlanc, G.; Williams, T.E.; Mattox, T.M.; Helms, B.A.; Milliron, D.J. Nanocomposite architecture for rapid, spectrally-selective electrochromicmodulation of solar transmittance. *Nano Lett.* **2015**, *15*, 5574–5579. [CrossRef] [PubMed]
9. Zeb, S.; Sun, G.; Nie, Y.; Xu, H.; Cui, Y.; Jiang, X. Advanced developments in nonstoichiometric tungsten oxides for electrochromic applications. *Mater. Adv.* **2021**, *2*, 6839–6884. [CrossRef]
10. Barile, C.J.; Slotcavage, D.J.; McGehee, M.D. Polymers in nonstoichiometric tunic materials that selectively modulate visible and near-infrared light. *Chem. Mater.* **2016**, *28*, 1439–1445. [CrossRef]
11. Khandelwal, H.; Schenning, A.P.H.J.; Debije, M.G. Infrared regulating smart window based on organic materials. *Adv. Energy Mater.* **2017**, *7*, 1602209. [CrossRef]
12. Garcia, G.; Buonsanti, R.; Llordes, A.; Runnerstrom, E.L.; Bergerud, A.; Milliron, D.J. Near-infrared spectrally selective plasmonic electrochromic thin films. *Adv. Opt. Mater.* **2013**, *1*, 215–220. [CrossRef]
13. Garcia, G.; Buonsanti, R.; Runnerstrom, E.L.; Mendelsberg, R.J.; Llordes, A.; Anders, A.; Richardson, T.J.; Milliron, D.J. Dynamically modulating the surface plasmon resonance of doped semiconductor nanocrystals. *Nano Lett.* **2011**, *11*, 4415–4420. [CrossRef] [PubMed]
14. Maiorov, V.A. Electrochromic glasses with separate regulation of transmission of visible light and near-infrared radiation (review). *Opt. Spectrosc.* **2019**, *126*, 412–430. [CrossRef]
15. Li, N.; Chang, T.; Gao, H.; Gao, X.; Ge, L. Morphology-controlled $WO_{3-x}$ homojunction: Hydrothermal synthesis, adsorption properties, and visible-light-driven photocatalytic and chromic properties. *Nanotechnology* **2019**, *30*, 415601. [CrossRef]
16. Drmosh, Q.A.; Al-Muhaish, N.A.; Al Wajih, Y.A.; Alam, M.W.; Yamani, Z.H. Surface composite and morphology tuning of tungsten oxide thin films for acetone gas sensing. *Chem. Phys. Lett.* **2021**, *776*, 138659. [CrossRef]
17. Wang, G.; Ling, Y.; Wang, H.; Yang, X.; Wang, C.; Zhang, J.Z.; Li, Y. Hydrogen-treated $WO_3$ nanoflakes show enhanced photostability. *Energy Environ. Sci.* **2012**, *5*, 6180–6187. [CrossRef]
18. Castro-García, S.; Pecquenard, B.; Bender, A.; Livage, J.; Julien, C. Electrochromic Properties of Tungsten Oxides Synthesized from Aqueous Solutions. *Ionics* **1997**, *3*, 104–109. [CrossRef]
19. Alam, M.W.; Wang, Z.; Naka, S.; Okada, H. Performance enhancement of top-contact pentacene-based organic thin-film transistors with bilayer $WO_3$/Au electrodes. *Jpn. J. Appl. Phys.* **2013**, *52*, 03BB08. [CrossRef]
20. Zhou, D.; Xie, D.; Shi, F.; Wang, D.H.; Ge, X.; Xia, X.H.; Wang, X.L.; Gu, C.D.; Tu, J.P. Crystalline/amorphous tungsten oxide core/shell hierarchical structures and their synergistic effect for optical modulation. *J. Colloid Interface Sci.* **2015**, *460*, 200–208. [CrossRef]
21. Wei, W.; Li, Z.; Guo, Z.; Li, Y.; Hou, F.; Guo, W.; Wei, A. An electrochromic window based on hierarchical amorphous $WO_3/SnO_2$ nanoflake arrays with boosted NIR modulation. *Appl. Surf. Sci.* **2022**, *571*, 151277. [CrossRef]
22. Cai, G.F.; Zhou, D.; Xiong, Q.Q.; Zhang, J.H.; Wang, X.L.; Gu, C.D.; Tu, J.P. Efficient electrochromic materials based on $TiO_2$@$WO_3$ core/shell nanorod arrays. *Sol. Energy Mater. Sol. Cells* **2013**, *117*, 231–238. [CrossRef]

23. Cai, G.-F.; Wang, X.-L.; Zhou, D.; Zhang, J.-H.; Xiong, Q.-Q.; Gu, C.-D.; Tu, J.-P. Hierarchical structure Ti-doped $WO_3$ film with improved electrochromism in visible-infrared region. *Rsc Adv.* **2013**, *3*, 6896–6905. [CrossRef]
24. Xia, Z.-j.; Wang, H.-l.; Su, Y.-f.; Tang, P.; Dai, M.-j.; Lin, H.-j.; Zhang, Z.-g.; Shi, Q. Enhanced electrochromic properties by improvement of crystallinity for sputtered $WO_3$ film. *Coatings* **2020**, *10*, 577. [CrossRef]
25. Huang, Q.; Cao, S.; Liu, Y.; Liang, Y.; Guo, J.; Zeng, R.; Zhao, J.; Zou, B. Boosting the $Zn^{2+}$-based electrochromic properties of tungsten oxide through morphology control. *Sol. Energy Mater. Sol. Cells* **2021**, *220*, 110853. [CrossRef]
26. Mathuri, S.; Margoni, M.M.; Ramamurthi, K.; Babu, R.R.; Ganesh, V. Hydrothermal assisted growth of vertically aligned platelet like structures of $WO_3$ films on transparent conducting FTO substrate for electrochromic performance. *Appl. Surf. Sci.* **2018**, *449*, 77–91. [CrossRef]
27. Cai, G.F.; Tu, J.P.; Zhou, D.; Wang, X.L.; Gu, C.D. Growth of vertically aligned hierarchical $WO_3$ nano-architecture arrays on transparent conducting substrates with outstanding electrochromic performance. *Sol. Energy Mater. Sol. Cells* **2014**, *124*, 103–110. [CrossRef]
28. Wang, L.; Liu, Y.; Han, G.; Zhao, H. Controllable synthesis of hexagonal $WO_3$ nanorod-cluster films with high electrochromic performance in NIR range. *J. Alloy. Compd.* **2022**, *890*, 161833. [CrossRef]
29. Yang, L.; Ge, D.; Zhao, J.; Ding, Y.; Kong, X.; Li, Y. Improved electrochromic performance of ordered macroporous tungsten oxide films for IR electrochromic device. *Sol. Energy Mater. Sol. Cells* **2012**, *100*, 251–257. [CrossRef]
30. Zhang, G.; Xiao, X.; Li, B.; Gu, P.; Xue, H.; Pang, H. Transition metal oxides with one-dimensional/one-dimensional-analogue nanostructures for advanced supercapacitors. *J. Mater. Chem. A* **2017**, *5*, 8155–8186. [CrossRef]
31. Gao, T.; Jelle, B.P. Visible-light-driven photochromism of hexagonal sodium tungsten bronze nanorods. *J. Phys. Chem. C* **2013**, *117*, 13753–13761. [CrossRef]
32. Yuan, G.; Hua, C.; Khan, S.; Jiang, S.; Wu, Z.; Liu, Y.; Wang, J.; Song, C.; Han, G. Improved electrochromic performance of $WO_3$ films with size controlled nanorods. *Electrochim. Acta* **2018**, *260*, 274–280. [CrossRef]
33. Zhao, P.; Ye, X.; Zhu, Y.; Jiang, H.; Wang, L.; Yue, Z.; Wan, Z.; Jia, C. Three-dimensional ordered macroporous $NiFe_2O_4$ coated carbon yarn for knittable fibriform supercapacitor. *Electrochim. Acta* **2018**, *281*, 717–724. [CrossRef]
34. Ha, J.-H.; Muralidharan, P.; Kim, D.K. Hydrothermal synthesis and characterization of self-assembled h-$WO_3$ nanowires/nanorods using EDTA salts. *J. Alloy. Compd.* **2009**, *475*, 446–451. [CrossRef]
35. Wen, R.-T.; Granqvist, C.G.; Niklasson, G.A. Eliminating degradation and uncovering ion-trapping dynamics in electrochromic $WO_3$ thin films. *Nat. Mater.* **2015**, *14*, 996–1001. [CrossRef] [PubMed]
36. Li, J.; Zhu, J.; Liu, X. Synthesis, characterization and enhanced gas sensing performance of $WO_3$ nanotube bundles. *New J. Chem.* **2013**, *37*, 4241–4249. [CrossRef]
37. Zhang, X.; Dou, S.; Li, W.; Wang, L.; Qu, H.; Chen, X.; Zhang, L.; Zhao, Y.; Zhao, J.; Li, Y. Preparation of monolayer hollow spherical tungsten oxide films with enhanced near infrared electrochromic performances. *Electrochim. Acta* **2019**, *297*, 223–229. [CrossRef]
38. Zhao, Y.; Zhang, X.; Chen, X.; Li, W.; Wang, L.; Ren, F.; Zhao, J.; Endres, F.; Li, Y. Preparation of $WO_3$ films with controllable crystallinity for improved near-infrared electrochromic performances. *ACS Sustain. Chem. Eng.* **2020**, *8*, 11658–11666. [CrossRef]
39. Wang, Z.; Gong, W.; Wang, X.; Chen, Z.; Chen, X.; Chen, J.; Sun, H.; Song, G.; Cong, S.; Geng, F.; et al. Remarkable near-infrared electrochromism in tungsten oxide driven by interlayer water-induced battery-to-pseudocapacitor transition. *ACS Appl. Mater. Interfaces* **2020**, *12*, 33917–33925. [CrossRef] [PubMed]
40. Zhou, K.; Wang, H.; Zhang, S.; Jiu, J.; Liu, J.; Zhang, Y.; Yan, H. Electrochromic modulation of near-infrared light by $WO_3$ films deposited on silver nanowire substrates. *J. Mater. Sci.* **2017**, *52*, 12783–12794. [CrossRef]